Article

Unrecorded Tundra Fires in Canada, 1986–2022

Matthew G. Hethcoat [1,*] **, Piyush Jain** [1]**, Marc-André Parisien** [1]**, Rob Skakun** [1]**, Luka Rogic** [2] **and Ellen Whitman** [1]

[1] Northern Forestry Centre, Canadian Forest Service, Natural Resources Canada, 5320 122 Street NW, Edmonton, AB T6H 3S5, Canada; marc-andre.parisien@nrcan-rncan.gc.ca (M.-A.P.)

[2] Department of Electrical and Computer Engineering, University of British Columbia, 5500-2332 Main Mall, Vancouver, BC V6T 1Z4, Canada; rogluka@gmail.com

* Correspondence: matthew.hethcoat@nrcan-rncan.gc.ca

Abstract: Climate-driven changes in fire regimes are expected across the pan-Arctic region. Trends in arctic fires are thought to be generally increasing; however, fire mapping across the region is far from comprehensive or systematic. We developed a new detection workflow and built a dataset of unrecorded tundra fires in Canada using Landsat data. We built a reference dataset of spectral indices from previously mapped fires in northern Canada to train a Random Forest model for detecting new fires between 1986 and 2022. In addition, we used time series information for each pixel to reduce false positives and narrow the large search space down to a finite set of regions that had experienced changes. We found 209 previously undetected fires in the Arctic and sub-Arctic regions, increasing the mapped burned area by approximately 30%. The median fire size was small, with roughly 3/4 of the fires being <100 ha in size. The majority of newly detected fires (69%) did not have satellite-derived hotspots associated with them. The dataset presented here is commission error-free and can be viewed as a reference dataset for future analyses. Moreover, future improvements and updates will leverage these data to improve the detection workflow outlined here, particularly for small and low-severity fires. These data can facilitate broader analyses that examine trends and environmental drivers of fire across the Arctic region. Such analyses could begin to untangle the mechanisms driving heterogeneous fire responses to climate observed across regions of the Circumpolar North.

Keywords: Arctic; Google Earth Engine; hotspots; lightning; MODIS; NBAC; Normalized Burn Ratio; Random Forest; Tasseled Cap; VIIRS

1. Introduction

Empirical data and modeling indicate a growing likelihood of fire in the Arctic [1,2]. There are increasing trends in the length of the fire season [1,3], air temperature, fuel load and availability, and a host of fire-related abiotic factors in the Arctic and sub-Arctic zones [4–6]. While many northern regions are changing faster than those at lower- and mid-latitudes [2], global patterns of Arctic and tundra fire activity indicate substantial spatio-temporal variation in burning. Fires have increased in Alaska and Siberia [1,7], but a slight decreasing trend has been observed in the Northwest Territories of Canada [6,8].

The accurate spatio-temporal mapping of fires is fundamental to understanding changes in the burned area, fire severity, post-fire vegetation recovery, and for determining any climate- and human-driven changes in fire regimes globally. Furthermore, such maps offer an essential baseline from which to measure changes, particularly over periods in which rapid changes are forecasted. In recent decades, a suite of space-borne satellite sensors have facilitated large-scale fire monitoring and mapping, enabling a global-scale analyses of the patterns, trends, and drivers of wildfires [9,10]. Indeed, since approximately 1979, beginning with the Advanced Very High Resolution Radiometer, satellites have acquired sub-daily observations of fire activity [11]. However, many of the purpose-built fire products derived from thermal anomalies (referred to hereafter as hotspots) are spatially

coarse and thus cannot detect small fires nor delineate perimeters effectively to produce detailed burned area estimates. The Landsat missions, with their increased spatial resolution (over Moderate Resolution Imaging Spectroradiometer (MODIS) or Visible Infrared Imaging Radiometer Suite (VIIRS) sensors) and global coverage, have enabled a fine-tuned understanding of burn severity and area burned [12].

Canada has two federally maintained national fire databases—the Canadian National Fire Database (CNFDB) and the National Burned Area Composite (NBAC)—that collect fire data from a variety of sources (e.g., provincial and territorial agencies, federal departments and agencies, satellite mapping techniques, etc.). The CNFDB is composed of fire maps of varying quality, produced by jurisdictional fire management agencies and compiled into a single national database [13]. The NBAC uses a consistent methodology to detect and map new fires, as well as refine the perimeters of historic fires that were not accurately delineated within the CNFDB [13,14]. Critically, data from the NBAC are used by the government of Canada to report on progress toward international commitments to monitor anthropogenic emissions and are regarded as the authoritative source on more recent fires in Canada [15,16].

Historically, fire suppression activity has been absent or minimal in the remote northern areas of Canada and, consequently, fires that have occurred outside of forested regions (i.e., north of the treeline) or far from inhabited areas have not been monitored or mapped [17]. Indeed, the territory of Nunavut does not have a fire management agency. Moreover, even newer methodological techniques to improve fire mapping in Canada have limited their study domain to exclude regions north of the treeline (e.g., [13,18]). The omission is likely driven by assumptions about a lack of fire in the region and the fact that disturbance mapping in tundra environments is known to be extremely challenging with remotely sensed data [19]. Consequently, the NBAC and CNFDB do not represent a complete picture of fires in Canada and there is a clear gap in our understanding of fires in remote northern regions, particularly above the treeline.

The primary objective of this study was to detect and map unrecorded tundra fires within Canada using Landsat data. There is a growing need to assess and understand potential changes in fire regimes within Canada, particularly in light of the 2023 fire season, where a record-breaking area of >15 M ha burned [20]. Given the lack of systematic fire monitoring outside of forested regions, we sought to advance the build-out and maintenance of a more comprehensive accounting of fires in northern Canada since 1986.

2. Materials and Methods

2.1. Study Area

We focused on three ecozones in northern Canada [21] covering areas roughly north of the treeline—the Arctic Cordillera, Northern Arctic, and Southern Arctic ecozones (Figure 1). The study area stopped at approximately 74.5 degrees north (i.e., in the Arctic Ocean north of Banks, Victoria, Prince of Wales, Somerset, and the Baffin Islands). The vegetation present across the region is diverse and is generally north of the treeline, consisting of a combination of herbaceous plants, shrubs, mosses, and lichens (see [22] for a more complete breakdown of vegetation characteristic and communities present across the various subzones within the region). Across the study area, systematic fire monitoring has historically been of low priority. Although there are many small communities throughout, it is very sparsely populated. Land use mainly consists of low-impact traditional and cultural activities, with few permanent roads or energy corridors; however, various mines operate across the region.
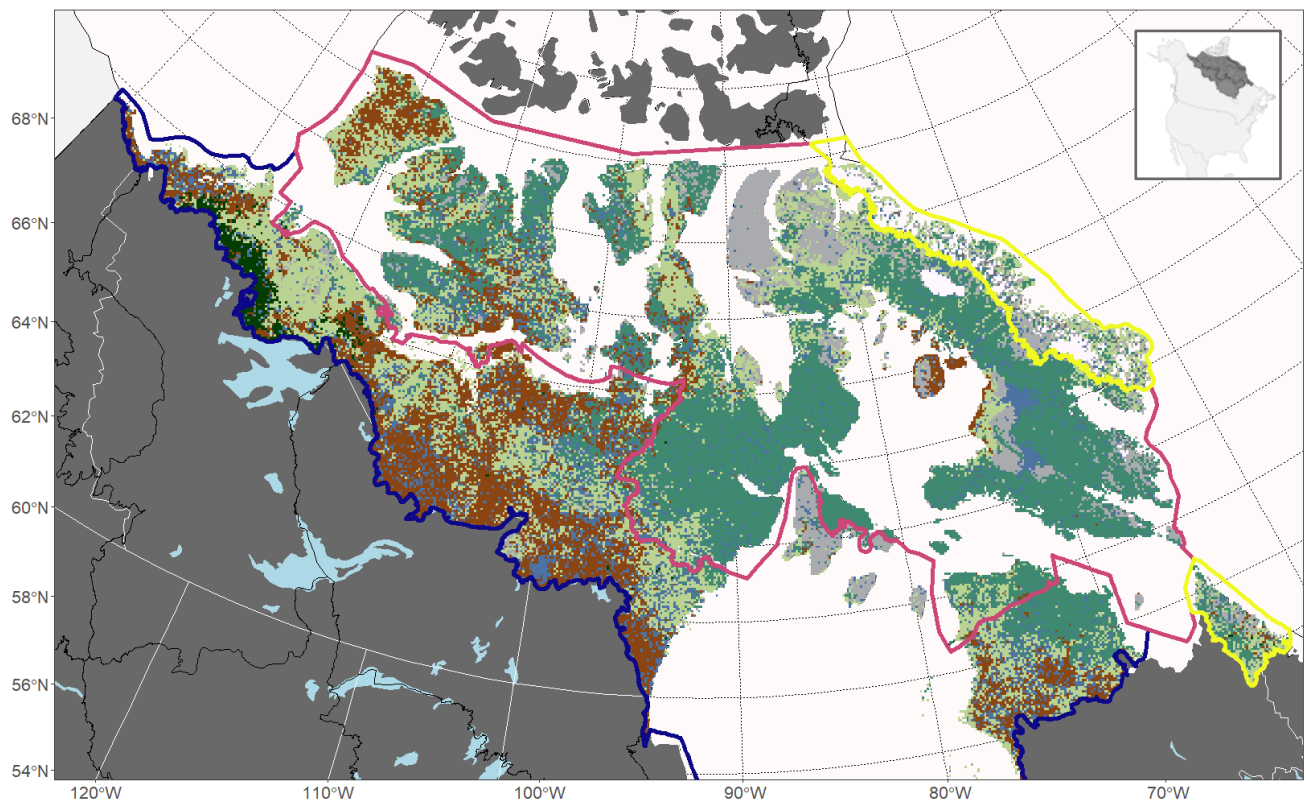
Figure 1. Canadian ecozones and broad land cover types (from North American Land Change Monitoring System [23]) over the study area searched for tundra fires between 1986 and 2022. The Southern Arctic is outlined in dark blue, the Northern Arctic is outlined in pink, and the Arctic Cordillera is outlined in yellow. Needleleaf forests are dark green, shrublands are brown, grassland-lichen-moss are light green, barren-lichen-moss are medium green, water and wetlands are blue, barren ground is light grey, and snow is white. Provincial and territorial borders are in white, major lakes are light blue, and ecozones outside the study area are outlined in black.

2.2. Detecting Fires

2.2.1. Datasets, Satellite Imagery, and Initial Modeling

We first sought to build a reference dataset of spectral fire indices (Tables A1 and A2) for northern Canada to assist with fire detection. We sampled burned and unburned point locations from all NBAC fires that occurred within the study area and the next adjacent ecozones south (i.e., the northernmost fires available) between 2014 and 2020 (n = 253). Most NBAC fires had 25 burned pixels and 30 unburned pixels randomly sampled, with unburned locations coming from within a 1 km buffer surrounding fire perimeters. More unburned pixels were sampled in an attempt to balance out sampling, because burned areas were usually larger and therefore had a smaller chance of containing masked water bodies, which resulted in failed sampling. We sampled differenced fire indices, subtracting imagery 1-year post-fire from 1-year pre-fire. Some smaller fires could not fit 25 burned and 30 unburned sample pixels (e.g., a fire less than two hectares has fewer than 25 pixels in the entire burn scar), and the final dataset contained 11,056 points, of which 4989 (45%) were unburned and 6067 (55%) were burned. These data were then used to train and validate a Random Forest (RF) model for detecting fires in our study area (details below).

We used Landsat (5, 7, 8, and 9) Collection 2 surface reflectance data in Google Earth Engine (GEE) to calculate spectral indices associated with fire mapping and vegetation change [24]. Pixels covered by clouds, shadows, snow, and water were removed using the quality flags provided within the QA_PIXEL band in Landsat Collection 2. A summer-season mosaic was generated for each year using the median of all available scenes between

15 June and 15 September. We removed permanent water bodies using the global water mask developed by the European Commission's Joint Research Centre [25].

Preliminary model training and testing was conducted in a Google Colaboratory notebook [26] to optimize RF tuning parameters and select fire indices that accurately classified burned areas (Tables A3 and A4). We used a suite of Scikit-learn [27] functions for model selection, feature reduction, and k-fold cross-validation to select a final RF model for efficient computation in GEE (Appendix B). The top RF model showed strong predictive performance during model validation (Table A4); however, during model deployment to the study area—a region not well represented in the training data—this model regularly predicted sparsely vegetated regions and atmospheric artifacts as having a high probability of being burned, despite having not experienced a fire (Figure 2). Through subsequent testing of candidate variables, we identified three metrics that maintained strong detection while greatly reducing spurious detections in our northern study area: Normalized Burn Ratio 2 (NBR2), Tasseled Cap Brightness (TCB), and Tasseled Cap Greenness (TCG, Figure 2, Table A4). This RF model was then used as part of the fire detection methodology detailed below.
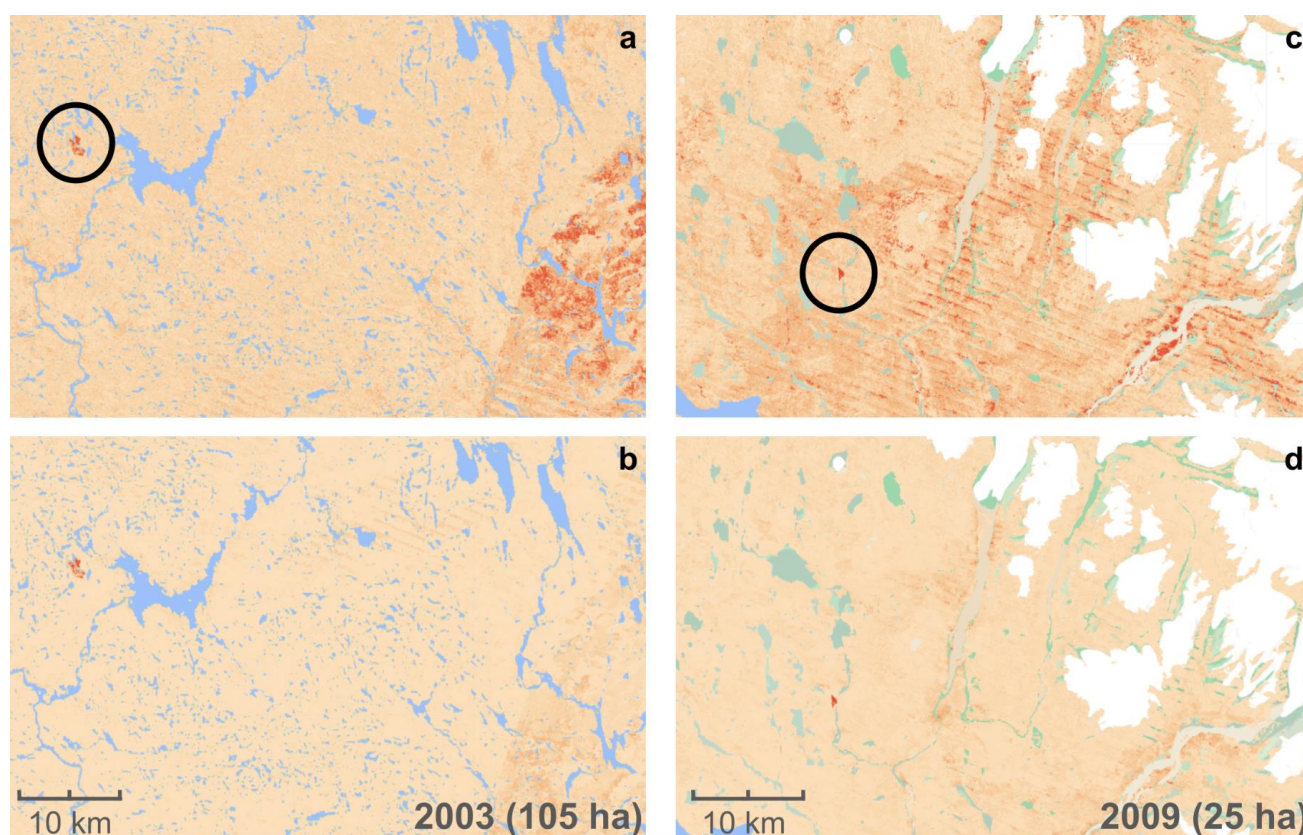

Figure 2. Comparison of Random Forest (RF) model predictions using the top-performing model during validation (**a**,**c**) versus the chosen model for the study area after further regional testing (**b**,**d**). Probability of being burned is displayed in shades of red, with darker red being higher probability of fire. The top images show higher incidences of false positives from insufficient cloud removal near the fires (circled in (**a**,**c**)). Noticeable banding present in imagery was a common artifact from the missing data in Landsat 7 scan-line corrector error images.

2.2.2. Fire Detection

We used a three-step workflow to map fires (Figure 3). First, candidate fire detections—pixels that met a four-rule criteria (details below)—were exported from GEE. Next, candidate fires were visually inspected to confirm a change event was fire-related, as changes in hydrology, thaw slumps, mining activities, road expansions, phenological differences, etc.

were frequently detected. Finally, we used R Statistical Computing Software, version 4.2.2 [28], to revisit confirmed fires and delineate a refined fire perimeter at 30-m resolution, utilizing the 'rgee' package [29]. This multi-stage approach was used to reduce the large search space down to a finite set of areas that had experienced change events and stay within the computation limits of GEE.
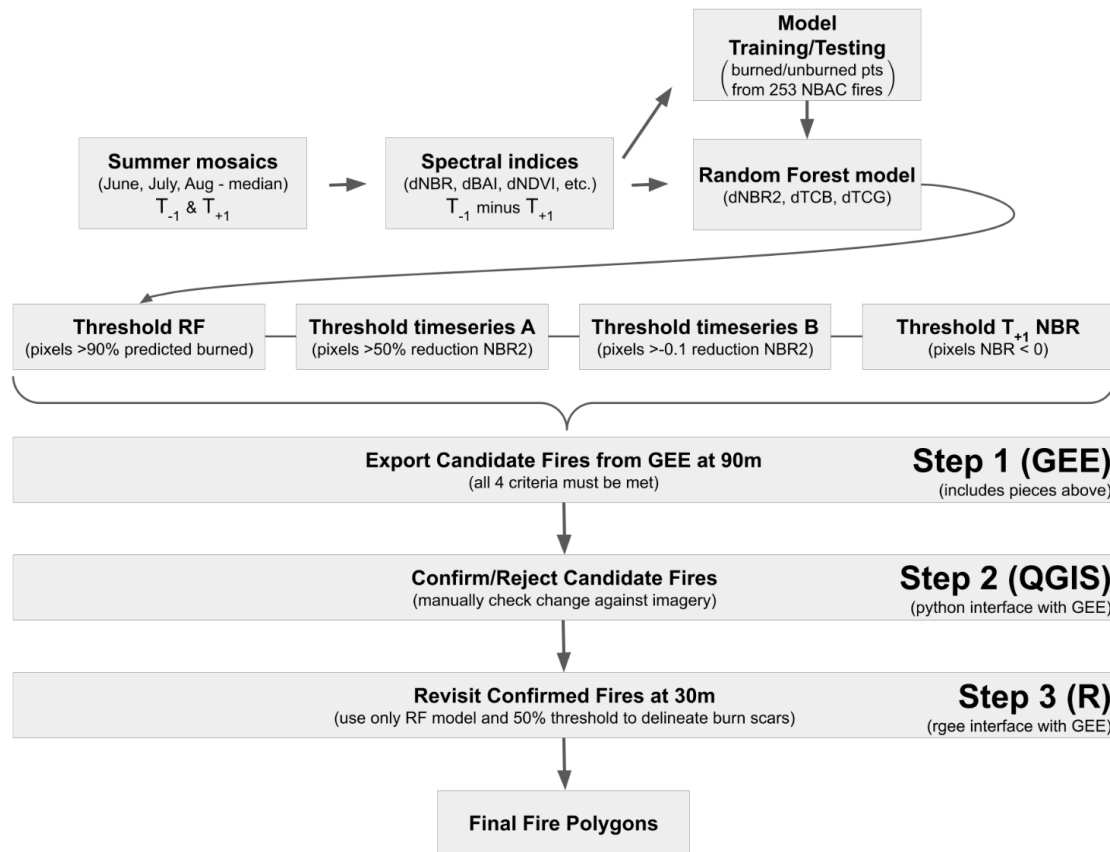

Figure 3. Fire detection workflow used to locate and confirm Canadian tundra fires between 1986 and 2022.

The first step in the multi-stage fire detection methodology was to identify candidate fires in GEE using a four-rule criteria. We used existing NBAC fire perimeters from within the study area to settle on the thresholds outlined below. The first criterion retained only pixels with $\geq 90\%$ of the RF votes identified as being burned. A high RF threshold maintained detection and reduced false positives in sparsely vegetated areas and pixels with insufficient cloud removal. Despite a high RF threshold, many false positives remained and we incorporated two additional rules based on time series information. Criteria two and three compared post-fire imagery to a pre-fire median of up to three years. For criterion two, pixels were retained if there was a >50% decrease in post-fire NBR2, compared to a three-year pre-fire median. Inter-annual differences in phenology and apparent drought stress resulted in NBR2 drops > 30% in some years; we sought to account for these variations. The third criterion required the difference between the post-fire NBR2 and the three-year pre-fire median to be ≤ -0.1. Again, inter-annual differences in seasonal mosaics resulted in NBR2 differences of $\cong 0$ and we wanted to exclude those occurrences as well. Finally, the post-fire NBR values needed to be <0. Candidate fires that met all four criteria were exported as vectors from GEE at 90 m spatial resolution (Figure 3). This spatial resolution (i.e., 90 m rather than 30 m) was required in order to stay within the computation limits of GEE, given the size of the study area.

The second step in the methodology required a visual inspection of each candidate fire ≥ four pixels in size (encompassing 50–100 candidate areas per year). Four pixels was chosen for a minimum size (approximately four hectares) because some atmospheric effects still satisfied the four criteria and resulted in isolated one- to two-pixel noise, particularly over snowy and alpine regions in the northeast of the study area. A single reviewer used a suite of custom GEE scripts to visualize a time series of imagery over each candidate fire to confirm a change event was associated with a fire. Examples of events that were not fire-related are widespread regional hydrological changes visible throughout the landscape, landslides or thaw slumps, and human footprint expansion through mining and road building. This manual validation step was preferred, rather than a fully automated workflow, because of the dynamic nature of the landscape—changes in hydrology, thaw slumps, mining activities, road expansion, etc., frequently satisfied the four-rule criteria.

We finalized perimeters for confirmed fire events using the RF model from step one; however, this time retaining pixels with ≥50% of the votes as burned for perimeter mapping. The 50% threshold was chosen by comparing a range of thresholds against existing NBAC fire perimeters from within the study area. In general, fire perimeters were generated via RF prediction on differenced fire imagery, subtracting 1-year pre-fire imagery from 1-year post-fire imagery. However, some small or low-severity (n ≅ 20) fire perimeters were output with null geometries (i.e., no pixels had ≥ 50% votes as burned because of rapid vegetation recovery), and 1-year pre-fire imagery was subtracted from year-of-fire in those cases.

2.3. Validation

We cross-referenced our dataset against two data sources: (1) existing fires within the NBAC dataset and (2) satellite-derived hotspots from MODIS Terra (MOD14A1), MODIS Aqua (MYD14A1), and VIIRS (VNP141A). Sixty-six fires within the study area were already in the NBAC database and we calculated the omission rate of known fires against our new dataset. When using hotspots, we searched for additional fires potentially missed by our methodology. We buffered each hotspot by 3 km and output any potential fire perimeters using the RF prediction, keeping pixels ≥ 50% class votes as burned. As Terra began acquiring data in 2000, Aqua in 2002, and VIIRS in 2012, hotspots were searched over this subset of the study period (i.e., 2000–2022).

3. Results

We detected 206 new fires in our study area between 1986 and 2022 using our workflow, with an additional 3 fires found during hotspot validation, for a total of 209 newly mapped fires. Thus, including the existing NBAC fires, the region had 275 documented fires over the study period (Figure 4). In the combined dataset, the median number of fires in a given year was five and the median annual burned area was 219 hectares. The median fire size was 22.6 hectares (bootstrapped 95% CI = 16.2–28.3 ha) and 210 of the 275 total fires were <100 ha in size. No fires were detected from any source in 2004 or 2005. In total, the new fires added approximately 12,622 ha (a 32.8% increase) to the previously known total for the region (38,470 ha).

Nearly half of the new fires were in the Arctic (n = 96; 45.9%), defined as latitudes above 66° N by the Arctic Monitoring and Assessment Programme (Figure 5). No new fires were found within the Arctic Cordillera ecozone, though a single fire from 2022 was already mapped in the NBAC (>3500 ha), inside Kuururjuaq National Park, QC, representing the lone fire in the region over the study period. The Northern Arctic ecozone had 41 fires, most generally southwest of Wager Bay, NU, except for 1 fire on Baffin Island in 2009 (25 ha) and another in the Qikiqtaaluk Region, NU in 2020 (2 ha). The majority of newly detected fires occurred in the Southern Arctic ecozone, with 168, spread across three general regions: (1) the western edge of the ecoregion—forming a strip between Great Bear Lake and Tuktoyaktuk, NT; (2) northwest of Hudson Bay; and (3) northern Quebec (Figure 5).
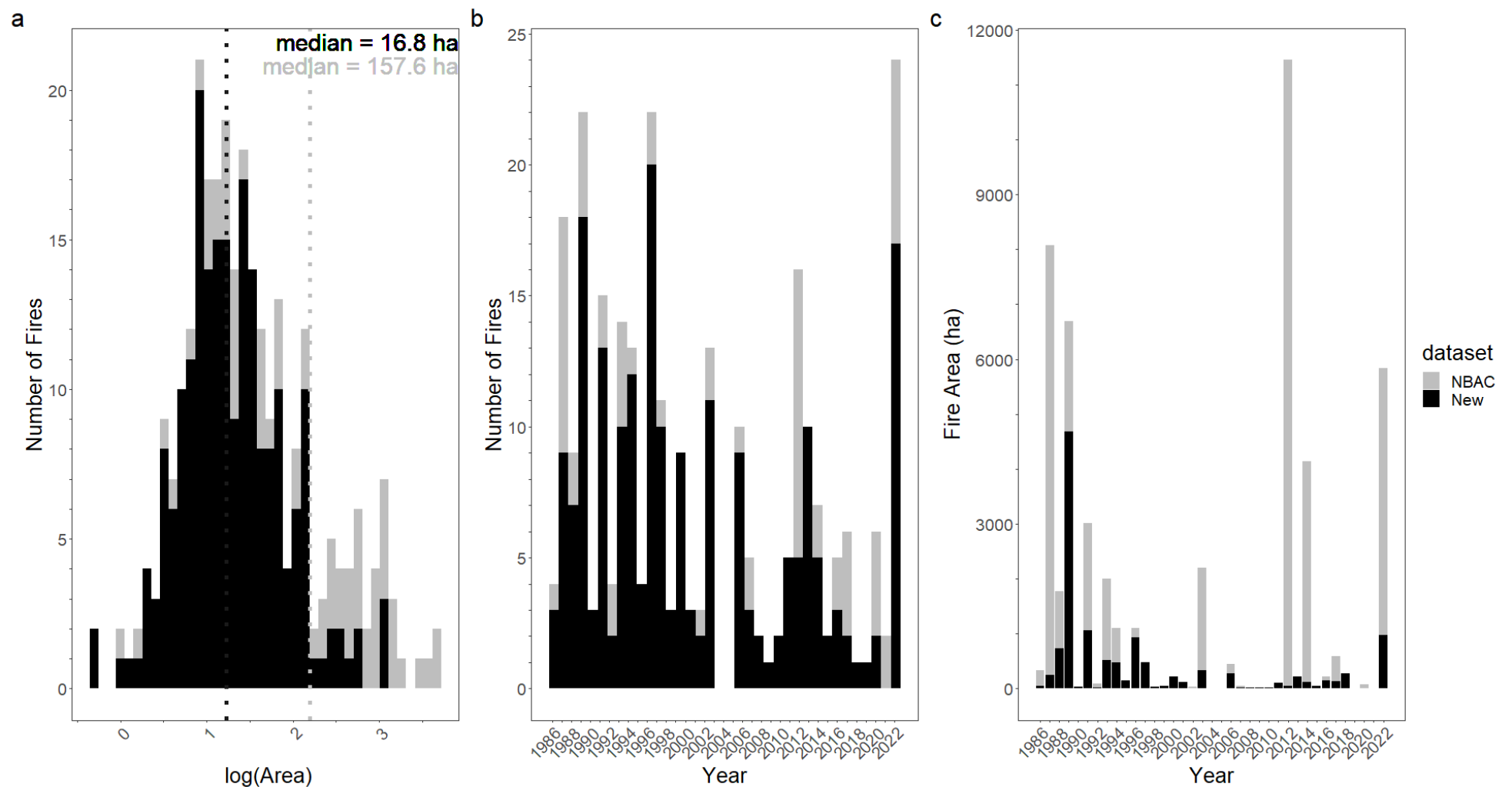
Figure 4. Distribution of (**a**) fire size in hectares, (**b**) number of fires per year, and (**c**) burned area per year within the study area from 1986 to 2022. The National Burned Area Composite (NBAC) data are in grey and the new fires detected in this study are in black, with the median fire size denoted by the vertical dashed lines (in (**a**)).
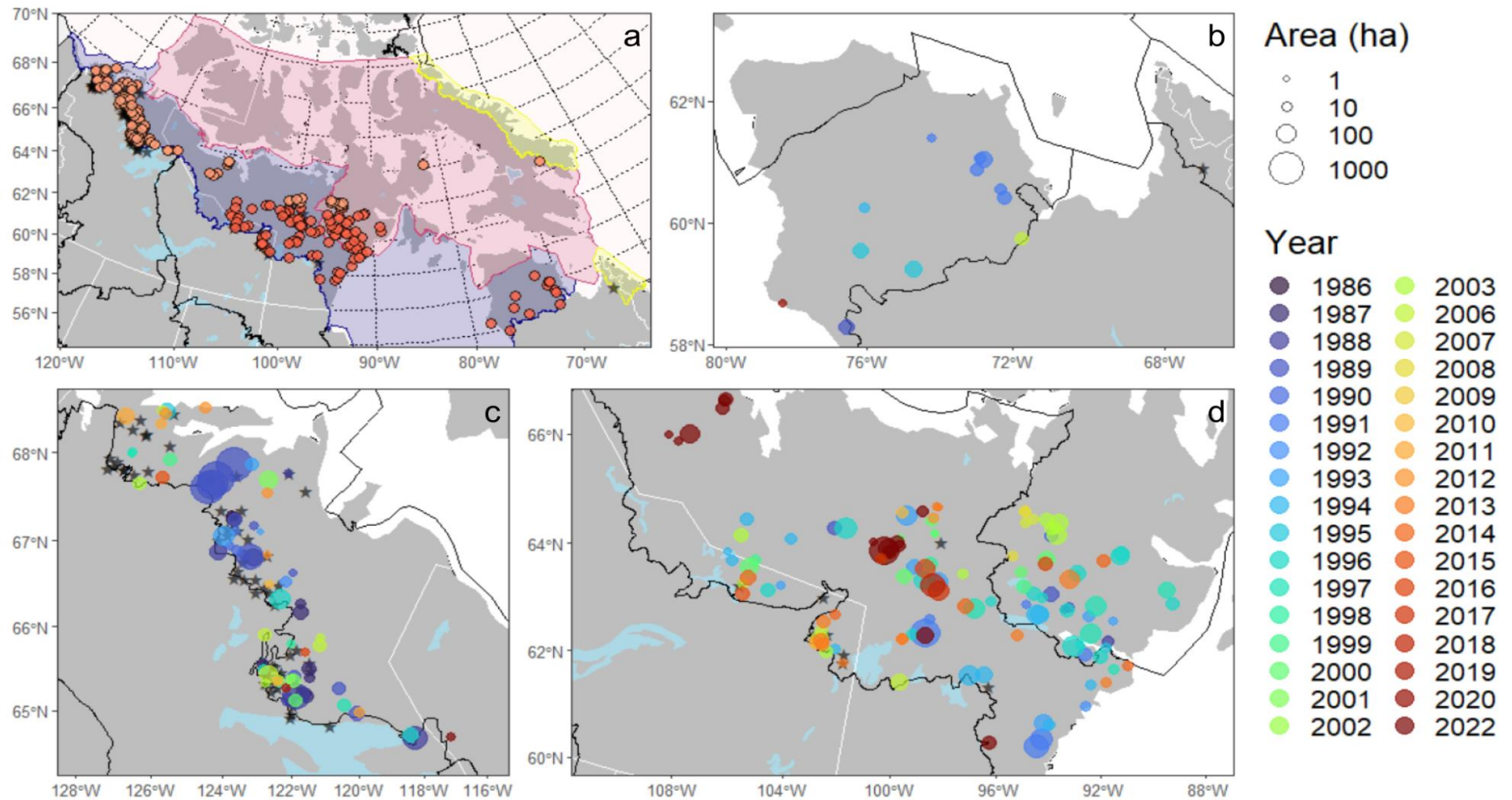
Figure 5. Spatial distribution of newly detected tundra fires that occurred between 1986 and 2022 (orange circles in (**a**), with individual fires north of 66°N shaded lighter orange. Fires previously mapped in the NBAC are black stars. Panels (**b**–**d**) are centered over each sub-region of fire clusters, showing the fire area as graduated point sizes and the year of burning as colors.

Of the 66 fires already in the NBAC database, our methodology failed to detect 5 (i.e., an 7.6% omission rate), with areas of approximately 9.4, 4.5, 3.4, 1.9, and 0.9 hectares. In terms of omission of the burned area, those five fires accounted for 0.05% of the total burned area previously mapped (approximately 20 ha out of 38,470). Using satellite-derived hotspots between 2002 and 2022, we found three additional fires missed by our methodology, with areas of approximately 12, 8, and 8 hectares. The majority of the fires already in the NBAC database had hotspots associated with them (60.1%), reflecting one of the ways these fires have historically been detected and mapped; however, an additional 15 fires in the NBAC database did not have any hotspots and were likely opportunistically found due to their proximity to other fires targeted for mapping. In contrast, 69.5% of the newly detected fires with our method did not have any hotspots associated with them (Table 1). The median fire size was larger for fires that had hotspots (64.3 ha) compared to those without (13.4 ha) and all fires >~150 ha had hotspots.

Table 1. Presence of thermal anomalies (i.e., hotspots) for fires within the study region, 2000–2022.

Hotspots Present	NBAC Fire	New Fire
Yes	23	29
No	15	66

4. Discussion

Satellite data are critical for monitoring fire dynamics globally, particularly in remote regions faced with rapid climate- and human-driven changes. We used Landsat imagery to generate a dataset of wildfires for the tundra region of Canada since 1986, increasing the known burned area by about 30%. In general, we did not find widespread, unaccounted-for burning across the study area. In an average year (i.e., median), the region—an area only slightly smaller than Argentina—had five fires and burned roughly 200 ha.

The approach outlined here combines elements, conceptually, from existing methods used to map fires in Canada [13,14,30]; however, some adjustments were made to tailor the detection approach to the study region. Specifically, our RF model (i.e., criterion 1) used bi-temporal Landsat imagery to detect changes in fire indices, akin to [13] and [14], but our approach used multiple indices (dNBR2, dTCB, and dTCG) and RF modeling as opposed to thresholding dNBR values. Similarly, changes in pixel value time series (i.e., criteria 2 and 3) are analogous to the breakpoint methods used by Hermosilla et al. [30] to detect fires, albeit much simplified to efficiently run in GEE. Moreover, we chose to use a multi-stage approach, whereby candidate fires were examined individually and re-mapped at a finer scale if confirmed, because attempts to produce a fully automated workflow (like the approaches referenced above) persistently included land-use and land-cover changes that were not fire-related (e.g., thaw slumps, road development, mine expansion, hydrologic changes). Thus, our methodological adjustments were focused on reducing false positives and producing a commission error-free dataset.

Our RF model used three spectral indices less commonly used (dNBR2, dTCB, and dTCG) for fire mapping (but see [31–34]). During model development and training we assessed many of the spectral indices commonly used for mapping fire perimeters and characterizing burn severity. However, during model deployment across our study area, we found that two of the tasseled cap bands (brightness and greenness) and NBR2 performed well at reducing false positives (Figure 2). NBR2 is known to penetrate smoke and clouds effectively, because of the incorporation of longer wavelength bands in the calculation [34], and is likely one of the major contributions to the reduction in false positives observed (Figure 2). In addition, NBR2 has been shown to perform better at detecting surface fires, relative to NBR [35], and might explain why NBR performed well during model training but NBR2 performed better over the study area. That is, the majority of the training data came from northern boreal fires and were thus trained and validated against spectral characteristics of forest fires, whereas surface fires were more common across the study area.

Tasseled cap indices (TCs), particularly brightness and greenness, have a long history in change detection applications across a variety of ecosystems [31,32], but are more often used to model post-fire recovery trajectories rather than map fire perimeters [36]. However, a number of studies from high latitudes have highlighted the usefulness of TCs for mapping fires [32,33,37]. TCs calculations decompose the visible, near-infrared, and short-wave infrared Landsat bands (n = 6) into three orthogonal bands and thus provide information about spectral changes across the full range of reflectance values (i.e., dimensionality reduction). Consequently, because TCs were not derived for a particular vegetation type, biome, or range of the electromagnetic spectrum measured using Landsat, they are likely sensitive to changes across diverse vegetation types present in tundra environments [32,37]. For example, the spectral signatures of nonvascular plants (e.g., Bryophytes) and lichens can be significantly influenced by moisture content [19], with both photosynthetic activity and respiration tied to water availability. Given that this region lacks a strong reflectance signal from chlorophyll in tall vegetation, as relied on for fire mapping in more southern ecosystems, these alternate indices may be better suited to capture fire-induced change in low-vegetation and low-fuel environments.

Our finding that the majority of fires in the study area did not have hotspots associated with them aligns with other recent studies that have highlighted the lack of a thermal signal for smaller, high-latitude fires [38,39]. Moreover, it suggests that prior studies that have used hotspots to constrain their search for Arctic and/or tundra fires likely omitted many smaller fires [12,40,41]. The lack of reliable hotspots is precisely why we tailored our methodology to not rely on them as a data source. In mapping exercises, the omission of small fires (<100 ha) tends to be more problematic in regions where they account for a significant proportion of the total area burned [42]. Indeed, the 200+ additional fires we found amounted to an increased burned area of about 30%, whereas recent work in sub-Saharan Africa found small fires (<100 ha) added >80% to previously mapped totals [42]. The annual burned areas in the boreal and taiga regions of Canada tend to be dominated by a small number of large fires, with 90–95% of the burned area coming from 5–10% of fires annually [8,43,44]. Our dataset does not reflect this pattern as strongly, with >90% of the burned area coming from approximately 23% of the fires (62/275) and >75% of fires being <100 ha in size (210/275). Moreover, these proportions are probably conservative, because we surely omitted some small fires in this initial study.

Between 2012 and 2022—the study period during which both the VIIRS and MODIS sensors were operating in the region—we found an unexpected pattern in hotspot detections for the fires in our dataset (Table 2). In particular, the MODIS sensors were more likely to detect a fire, despite having a coarser spatial resolution than the VIIRS sensors (1 km versus 375 m). This was a somewhat surprising finding, as others have shown that the VIIRS I-Band offers an improvement over the MODIS sensors in detection efficiency for small fires in other high-latitude and low-biomass regions [45,46]. We initially thought this difference might be related to overpass time and, possibly, early detection of short, wind-driven burn events (as the Terra platform passes over the equator at approximately 10:30 a.m. local time, followed by one of the VIIRS platforms at 12:40 p.m., then both the Aqua platform and the second VIIRS platform at approximately 1:30 p.m.). However, of the seven fires only seen by the MODIS sensors, the two smallest fires were detected only by the Aqua platform—the platform more temporally matched with the VIIRS sensors. Thus, it seems unlikely that overpass timing was the cause. Canada's Arctic region is known to be extremely cloudy [47,48], and it is also possible that differences in cloud masking procedures between the two sensors resulted in altered detection efficiencies.

Table 2. Summary of thermal anomalies detected by the MODIS and VIIRS satellite sensors between 2012 and 2022 (i.e., the study period during which both sensors were operational). All fire sizes are listed for MODIS and VIIRS, but only the smallest five detected by both sensors and the largest five neither sensor detected are listed. Superscripts [a] and [t] (for MODIS) indicate if the fire was exclusively detected by the Aqua or Terra platform, respectively (with no subscript representing detection by both platforms).

Detected by	Count	Sizes (ha)
Both	25	[3.4, 21.4, 25.2, 25.8, 32.0]
MODIS only	7	[1.9 [a], 8.6 [a], 12.4, 15.0, 26.8 [t], 38.8 [t], 66.3]
VIIRS only	2	[10.1, 12.3]
Neither	46	[45.1, 102.5, 109.2, 130.3, 131.5]

An alternative explanation may be due to the higher fire radiative power (FRP) detected by the MODIS sensors at northern latitudes [49]. While FRP is not part of the detection algorithm on its own, it is calculated directly from brightness values (in Kelvin) detected by each sensor [49]. Thus, the relatively lower FRP (which is derived from brightness) observed by the VIIRS sensor, suggests it is possible that the VIIRS fire detection algorithm may be unintentionally calibrated in a manner that misses fires in this region. Specifically, the VIIRS and MODIS fire-detection algorithms are similar at their core—both relying on the MODIS C6 algorithm—but the VIIRS algorithm separates fire pixels from background pixels using only the fixed thresholds test (see [50]), while the MODIS algorithm uses the same fixed thresholds test but also incorporates a newer dynamic threshold test [49–51]. Indeed, a post-hoc examination of the archived near-real-time Fire Information for Resource Management System (FIRMS) Global VIIRS and MODIS data [52] over fires observed by both sensors found generally higher brightness values for the MODIS sensors and a consistent saturation from the VIIRS sensors (Figure 6a). Moreover, given brightness is constrained onboard VIIRS, there is a resulting disconnect in the relationship between brightness and FRP (Figure 6b).
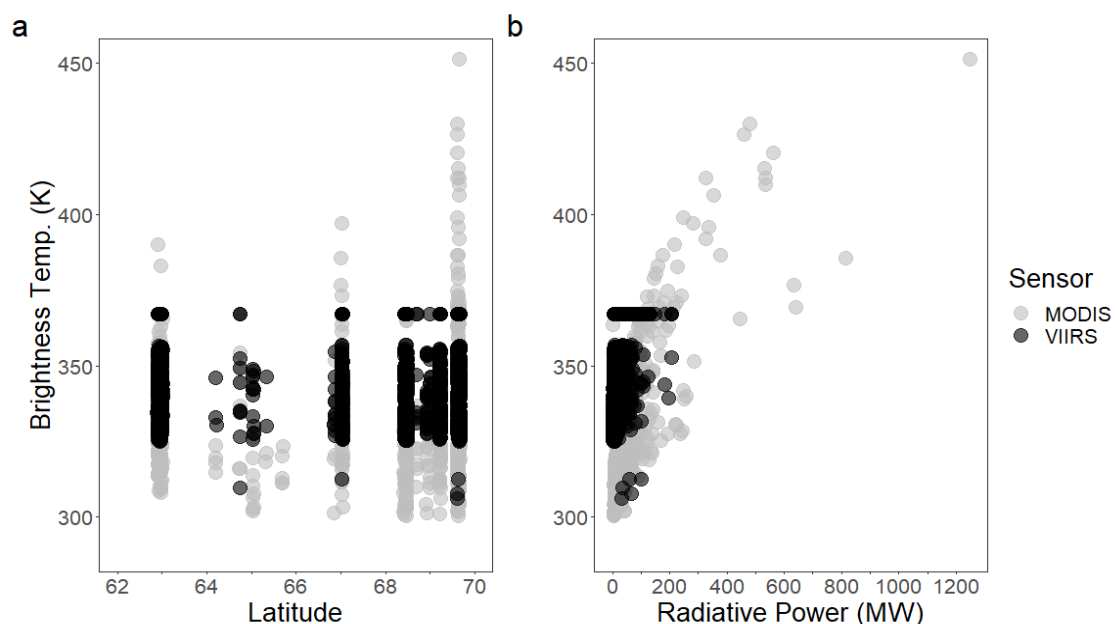

Figure 6. Brightness values recorded for VIIRS (black) and MODIS (grey) over tundra fires both sensors detected between 2012 and 2020 (**a**). Relationship between detected brightness and fire radiative power (**b**).

We were unable to distinguish the cause of the fire ignitions (human or lightning caused) with the data available. Future analyses using data from the Canadian Lightning Detection Network [53] may enable some discrimination between human- and lightning-caused fires for the region. Fire occurrence in Arctic Canada is determined using a mix of top-down (weather) and bottom-up (fuel) controls, with weather being particularly important [54]. As anthropogenic climate change has created severe warming in the Arctic [55], there have been observations of increasing fuel availability from taller and more productive vegetation [56] and an increase in fire-conducive weather conditions [57]. With increasing fuel and worsening fire weather acting as dual positive feedbacks to fire in this region, our findings further highlight the importance of monitoring and continued research to better understand arctic fire regimes, where a few small fires could shift to become a much more substantial area burned, if thresholds are surpassed [58]. Although none have been reported in recent decades, the potential for large (e.g., >1000 ha) wildfires likely exists across large parts of the study area. Neighboring Alaska has experienced a number of significant tundra wildfires in recent decades, including one > 100,000 ha [59]. While the conditions conducive to tundra wildfires of this extent are unlikely in much of the Canadian tundra, a formal examination of wildfire potential in this biome represents an important future area of research.

5. Limitations

While our results represent a step toward providing a more complete picture of burning over the preceding decades, we almost certainly missed some small fires, particularly in light of the frequency of smaller fires in the data (e.g., nearly 1/3 of fires were ≤10 ha; Figure 1a). Our method only examined candidate fires that were exported at 90 m pixel resolution and were at least 4 connected pixels in size. This resolution was initially determined with GEE computation limitations, but we continue to work toward the goal of using the native Landsat pixel size (i.e., 30 m) in future versions to more consistently identify smaller fires. The use of smaller pixels may help maintain the connectedness of burned patches, ensuring they are of sufficient size to be verified by the methodology. For example, a long, narrow fire might not have had four connected pixels, whereas a small circular one would be more likely to be connected. In addition, the patchiness of fire intensity would also influence whether four contiguous pixels met the criteria—even if more than four pixels fell within what would ultimately have formed the fire perimeter. Consequently, future versions will use native Landsat resolution and refine the criteria around the minimum connected pixels for examining candidate fires.

We used a somewhat conservative study area and could have extended the study domain farther south and undoubtedly map more fires missing from the NBAC database. We opted to initially focus on the Arctic and sub-Arctic regions because these have been left out of recent advances in automated burn mapping for Canada [13,18,30]. The region's exclusion has been, in part, the result of prior assumptions about a lack of fire in the region. In addition, disturbance mapping in the tundra is notoriously challenging with remotely sensed data [19] and is likely another reason the area has been omitted from so many mapping exercises over the years. The spectral signature of tundra environments is highly sensitive to species and community composition, inter- and intra-seasonal phenological events, and a host of abiotic factors [19,60]. Collectively, this has made automated disturbance mapping for the region fraught with commission and omission errors and is precisely why we included a manual validation step in our initial workflow. There are certainly more fires that still need to be folded into the NBAC database; however, the dataset here can be used to build an improved workflow with training data from a broader area, now that a more robust dataset of fires exists for the region.

6. Conclusions

The global Arctic and sub-Arctic are undergoing unprecedented changes. Continued warming has the potential to increase fire risk in the Arctic via increased lightning, increased

human activity, drying of peatlands, migration of fuels (e.g., northern advance of the treeline), altered species composition, and more [1,3,4,61]. Yet, the region will likely see the continued thawing of permafrost, increased variability in rainfall, and shifting hydrology [4,62], and so the extent to which these myriad changes will interact and how burning will be impacted remains unknown. Moreover, given recent findings that tundra fire locations are more likely to become major methane sources [63], as a consequence of permafrost thaw, the climate implications of increased fire activity are vital to understand. Regardless of the pattern or trend in future burning, accurate historical mapping of Arctic and sub-Arctic fires is a critical first step to understand potential changes in fire regimes. The dataset presented here can be viewed as a reference or benchmark dataset for future analyses to characterize trends and drivers of fire across the region or to assess impacts to ecosystem functions and recovery. Such analyses could begin to untangle the mechanisms driving heterogeneous fire responses observed between Alaska, Canada, and Russia [3].

Appendix A

Table A1. Landsat band abbreviations used in equations within Table A2.

Band Name	Band Abbreviation	Spectral Range (nm)	Band Number Landsat-89	Band Number Landsat-457
Blue	B	450–530	B2	B1
Green	G	510–600	B3	B2
Red	R	620–690	B4	B3
NIR	N	760–900	B5	B4
SWIR 1	S1	1550–1750	B6	B5
SWIR 2	S2	2080–2350	B7	B7

Table A2. Equations for fire indices used in Random Forest models built for fire detection (double asterisk represents exponentiation). Tasseled Cap coefficients are from [64].

Index Name	Equation
Bare Soil Index (BSI)	$((R + S1) - (N + B))/((R + S1) + (N + B))$
Burned Area Index (BAI)	$1/((0.1 - R)**2 + (0.06 - N)**2)$
Burned Area Index Modified SWIR (BAIMs)	$1/((N - 0.05 * N)**2 + (S1 - 0.2 * S1)**2)$
Char Soil Index (CSI)	$N/S1$
Enhanced Vegetation Index (EVI)	$2.5 * ((N - R)/(N + (6 * R) - (7.5 * B) + 1))$
Mid-Infrared Burn Index (MIRBI)	$((10 * S2) - (9.8 * S1) + 2)$
Modified Soil-Adjusted Vegetation Index (MSAVI)	$(2 * N + 1 - \mathrm{sqrt}((2 * N + 1)**2 - 8 * (N - R)))/2$
Normalized Burn Ratio (NBR)	$(N - S2)/(N + S2)$
Normalized Burn Ratio 2 (NBR2)	$(S1 - S2)/(S1 + S2)$
Normalized Difference Moisture Index (NDMI)	$(N - S1)/(N + S1)$
Normalized Difference Vegetation Index (NDVI)	$(N - R)/(N + R)$
Normalized Difference Water Index (NDWI)	$(G - N)/(G + N)$
Relativized Burn Ratio (RBR)	$dNBR/(NBR_{prefire} + 1.001)$
Relativized delta Normalized Burn Ratio (RdNBR)	$dNBR/|(NBR_{prefire})|**0.5$
Tasseled Cap Brightness (TCB)	$0.2043 * B + 0.4158 * G + 0.5524 * R + 0.5741 * N + 0.3124 * S1 + 0.2303 * S2$
Tasseled Cap Greenness (TCG)	$-0.1603 * B - 0.2819 * G - 0.4934 * R + 0.7940 * N - 0.0002 * S1 - 0.1446 * S2$
Tasseled Cap Wetness (TCW)	$0.0315 * B + 0.2021 * G + 0.3102 * R + 0.1594 * N - 0.6806 * S1 - 0.6109 * S2$

Appendix B

Preliminary model training and testing was conducted in a Google Colaboratory notebook [26] to optimize RF tuning parameters and select fire indices that accurately classified burned areas. We explored different combinations of hyperparameters using a suite of tools from scikit-learn [27]. Initially, we ran 100 different permutations with RandomizedSearchCV to find hyperparameters. Next we used GridSearchCV to exhaustively search over a narrower range of hyperparameters identified by RandomizedSearchCV. We then used RFECV to find the optimal set of features via Recursive feature elimination with cross-validation. We performed a 5-fold cross-validation, using RepeatedStratifiedKFold, to test optimal hyperparameter and feature selection vs. the base RandomForestClassifier model with all variables. At each point, we compared model accuracy against the same model using only 100 trees to assess the accuracy of a model with shorter computation time (Tables A3 and A4). Similarly, we compared the optimal model against a model that used the three best predictors, calculated using the gini criterion, to assess the accuracy of a model with an even shorter computation time (Table A4). Finally, after initial model deployment, persistent false positives were further reduced using a subset of indices (i.e., tundra variables in Table A4).

Table A3. Model sets and hyperparameters used to detect fires in Random Forest models. Tuning parameters from only the highest performing model are listed and were used across all final model sets.

Model Set	Variables
All variables	All indices from Table A2
Reduced variable set	dBAI, dBAIMs, dBSI, dCSI, dMSAVI, dNBR, dNBR2, dNDVI, dNDWI, dTCB, RBR, RdNBR
3 Best variables	dNBR, RBR, RdNBR
Tundra variables	dNBR2, dTCB, dTCG
Final hyperparameters	n_estimators = 100, min_samples_leaf = 1, max_samples = 0.7, max_leaf_nodes = 580, max_features = 'sqrt'

Table A4. Average of 5-fold cross-validation from Random Forest models built in Google Colaboratory using randomly sampled burned and unburned points from 253 fires in northern Canada 2014–2020.

Model Set	Precision	Recall	Overall Accuracy
All variables, 800 trees	0.94131	0.85997	0.89370
All variables, 100 trees	0.94095	0.85917	0.89309
Reduced variable set, 800 trees	0.93953	0.86082	0.89318
Reduced variable set, 100 trees	0.93820	0.86026	0.89217
3 Best variables, 800 trees	0.90695	0.83494	0.86239
3 Best variables, 100 trees	0.90565	0.83514	0.86176
Tundra variables, 800 trees	0.90068	0.83451	0.85865
Tundra variables, 100 trees	0.90001	0.83425	0.85769

References

1. Descals, A.; Gaveau, D.L.A.; Verger, A.; Sheil, D.; Naito, D.; Peñuelas, J. Unprecedented Fire Activity above the Arctic Circle Linked to Rising Temperatures. *Science* **2022**, *378*, 532–537. [CrossRef] [PubMed]
2. Walsh, J.E.; Ballinger, T.J.; Euskirchen, E.S.; Hanna, E.; Mård, J.; Overland, J.E.; Tangen, H.; Vihma, T. Extreme Weather and Climate Events in Northern Areas: A Review. *Earth-Sci. Rev.* **2020**, *209*, 103324. [CrossRef]
3. McCarty, J.L.; Aalto, J.; Paunu, V.-V.; Arnold, S.R.; Eckhardt, S.; Klimont, Z.; Fain, J.J.; Evangeliou, N.; Venäläinen, A.; Tchebakova, N.M.; et al. Reviews and Syntheses: Arctic Fire Regimes and Emissions in the 21st Century. *Biogeosciences* **2021**, *18*, 5053–5083. [CrossRef]
4. Berner, L.T.; Massey, R.; Jantz, P.; Forbes, B.C.; Macias-Fauria, M.; Myers-Smith, I.; Kumpula, T.; Gauthier, G.; Andreu-Hayles, L.; Gaglioti, B.V.; et al. Summer Warming Explains Widespread but Not Uniform Greening in the Arctic Tundra Biome. *Nat. Commun.* **2020**, *11*, 4621. [CrossRef] [PubMed]
5. Leipe, S.C.; Carey, S.K. Rapid Shrub Expansion in a Subarctic Mountain Basin Revealed by Repeat Airborne LiDAR. *Environ. Res. Commun.* **2021**, *3*, 071001. [CrossRef]
6. York, A.; Bhatt, U.S.; Gargulinski, E.; Grabinski, Z.; Jain, P.; Soja, A. *Wildland Fire in High Northern Latitudes*; Arctic Report Card, 2020, Thoman, R.L., Richter-Menge, J., Druckenmiller, M.L., Eds.; NOAA: Silver Spring, MD, USA, 2020.
7. Kasischke, E.S.; Verbyla, D.L.; Rupp, T.S.; McGuire, A.D.; Murphy, K.A.; Jandt, R.; Barnes, J.L.; Hoy, E.E.; Duffy, P.A.; Calef, M.; et al. Alaska's Changing Fire Regime—Implications for the Vulnerability of Its Boreal forests. *Can. J. For. Res.* **2010**, *40*, 1313–1324. [CrossRef]
8. Hanes, C.C.; Wang, X.; Jain, P.; Parisien, M.-A.; Little, J.M.; Flannigan, M.D. Fire-Regime Changes in Canada over the Last Half Century. *Can. J. For. Res.* **2019**, *49*, 256–269. [CrossRef]
9. Jones, M.W.; Abatzoglou, J.T.; Veraverbeke, S.; Andela, N.; Lasslop, G.; Forkel, M.; Smith, A.J.P.; Burton, C.; Betts, R.A.; van der Werf, G.R.; et al. Global and Regional Trends and Drivers of Fire Under Climate Change. *Rev. Geophys.* **2022**, *60*, e2020RG000726. [CrossRef]
10. Tyukavina, A.; Potapov, P.; Hansen, M.C.; Pickens, A.H.; Stehman, S.V.; Turubanova, S.; Parker, D.; Zalles, V.; Lima, A.; Kommareddy, I.; et al. Global Trends of Forest Loss Due to Fire From 2001 to 2019. *Front. Remote Sens.* **2022**, *3*, 825190. [CrossRef]
11. Wooster, M.J.; Roberts, G.J.; Giglio, L.; Roy, D.P.; Freeborn, P.H.; Boschetti, L.; Justice, C.; Ichoku, C.; Schroeder, W.; Davies, D.; et al. Satellite Remote Sensing of Active Fires: History and Current Status, Applications and Future Requirements. *Remote Sens. Environ.* **2021**, *267*, 112694. [CrossRef]
12. Talucci, A.C.; Loranty, M.M.; Alexander, H.D. Siberian Taiga and Tundra Fire Regimes from 2001–2020. *Environ. Res. Lett.* **2022**, *17*, 025001. [CrossRef]
13. Skakun, R.; Castilla, G.; Metsaranta, J.; Whitman, E.; Rodrigue, S.; Little, J.; Groenewegen, K.; Coyle, M. Extending the National Burned Area Composite Time Series of Wildfires in Canada. *Remote Sens.* **2022**, *14*, 3050. [CrossRef]
14. Hall, R.J.; Skakun, R.S.; Metsaranta, J.M.; Landry, R.; Fraser, R.H.; Raymond, D.; Gartrell, M.; Decker, V.; Little, J.; Hall, R.J.; et al. Generating Annual Estimates of Forest Fire Disturbance in Canada: The National Burned Area Composite. *Int. J. Wildland Fire* **2020**, *29*, 878–891. [CrossRef]
15. Kurz, W.A.; Apps, M.J. Developing Canada's National Forest Carbon Monitoring, Accounting and Reporting System to Meet the Reporting Requirements of the Kyoto Protocol. *Mitig. Adapt. Strateg. Glob. Chang.* **2006**, *11*, 33–43. [CrossRef]
16. Metsaranta, J.M.; Shaw, C.H.; Kurz, W.A.; Boisvenue, C.; Morken, S. Uncertainty of Inventory-Based Estimates of the Carbon Dynamics of Canada's Managed Forest (1990–2014). *Can. J. For. Res.* **2017**, *47*, 1082–1094. [CrossRef]
17. Tymstra, C.; Stocks, B.J.; Cai, X.; Flannigan, M.D. Wildfire Management in Canada: Review, Challenges and Opportunities. *Prog. Disaster Sci.* **2020**, *5*, 100045. [CrossRef]
18. Hermosilla, T.; Wulder, M.A.; White, J.C.; Coops, N.C.; Hobart, G.W.; Campbell, L.B. Mass Data Processing of Time Series Landsat Imagery: Pixels to Data Products for Forest Monitoring. *Int. J. Digit. Earth* **2016**, *9*, 1035–1054. [CrossRef]

19. Nelson, P.R.; Maguire, A.J.; Pierrat, Z.; Orcutt, E.L.; Yang, D.; Serbin, S.; Frost, G.V.; Macander, M.J.; Magney, T.S.; Thompson, D.R.; et al. Remote Sensing of Tundra Ecosystems Using High Spectral Resolution Reflectance: Opportunities and Challenges. *J. Geophys. Res. Biogeosci.* **2022**, *127*, e2021JG006697. [CrossRef]

20. Canadian Interagency Forest Fire Centre (CIFFC). Available online: https://ciffc.ca/ (accessed on 20 October 2023).

21. Ecological Stratification Working Group. *A National Ecological Framework for Canada*; Centre for Land and Biological Resources Research: Hull, QC, Canada, 1996.

22. Walker, D.A.; Raynolds, M.K.; Daniëls, F.J.A.; Einarsson, E.; Elvebakk, A.; Gould, W.A.; Katenin, A.E.; Kholod, S.S.; Markon, C.J.; Melnikov, E.S.; et al. The Circumpolar Arctic Vegetation Map. *J. Veg. Sci.* **2005**, *16*, 267–282. [CrossRef]

23. Natural Resources Canada 2020 Land Cover of Canada. Available online: https://open.canada.ca/data/en/dataset/ee1580ab-a2 3d-4f86-a09b-79763677eb47 (accessed on 16 December 2023).

24. Gorelick, N.; Hancher, M.; Dixon, M.; Ilyushchenko, S.; Thau, D.; Moore, R. Google Earth Engine: Planetary-Scale Geospatial Analysis for Everyone. *Remote Sens. Environ.* **2017**, *202*, 18–27. [CrossRef]

25. Pekel, J.-F.; Cottam, A.; Gorelick, N.; Belward, A.S. High-Resolution Mapping of Global Surface Water and Its Long-Term Changes. *Nature* **2016**, *540*, 418–422. [CrossRef] [PubMed]

26. Bisong, E. Google Colaboratory. In *Building Machine Learning and Deep Learning Models on Google Cloud Platform: A Comprehensive Guide for Beginners*; Bisong, E., Ed.; Apress: Berkeley, CA, USA, 2019; pp. 59–64. ISBN 978-1-4842-4470-8.

27. Pedregosa, F.; Varoquaux, G.; Gramfort, A.; Michel, V.; Thirion, B.; Grisel, O.; Blondel, M.; Prettenhofer, P.; Weiss, R.; Dubourg, V. Scikit-Learn: Machine Learning in Python. *J. Mach. Learn. Res.* **2011**, *12*, 2825–2830.

28. R Core Team. *R: A Language and Environment for Statistical Computing*; R Foundation for Statistical Computing: Vienna, Austria, 2022.

29. Aybar, C.; Qiusheng, W.; Bautista, L.; Yali, R.; Barja, A. rgee: An R package for interacting with Google Earth Engine. *J. Open Source Softw.* **2020**, *5*, 2272. [CrossRef]

30. Hermosilla, T.; Wulder, M.A.; White, J.C.; Coops, N.C.; Hobart, G.W. An Integrated Landsat Time Series Protocol for Change Detection and Generation of Annual Gap-Free Surface Reflectance Composites. *Remote Sens. Environ.* **2015**, *158*, 220–234. [CrossRef]

31. Healey, S.; Cohen, W.; Zhiqiang, Y.; Krankina, O. Comparison of Tasseled Cap-Based Landsat Data Structures for Use in Forest Disturbance Detection. *Remote Sens. Environ.* **2005**, *97*, 301–310. [CrossRef]

32. Fraser, R.H.; Olthof, I.; Kokelj, S.V.; Lantz, T.C.; Lacelle, D.; Brooker, A.; Wolfe, S.; Schwarz, S. Detecting Landscape Changes in High Latitude Environments Using Landsat Trend Analysis: 1. Visualization. *Remote Sens.* **2014**, *6*, 11533–11557. [CrossRef]

33. Loboda, T.V.; French, N.H.F.; Hight-Harf, C.; Jenkins, L.; Miller, M.E. Mapping Fire Extent and Burn Severity in Alaskan Tussock Tundra: An Analysis of the Spectral Response of Tundra Vegetation to Wildland Fire. *Remote Sens. Environ.* **2013**, *134*, 194–209. [CrossRef]

34. Trigg, S.; Flasse, S. An Evaluation of Different Bi-Spectral Spaces for Discriminating Burned Shrub-Savannah. *Int. J. Remote Sens.* **2001**, *22*, 2641–2647. [CrossRef]

35. French, N.H.F.; Graham, J.; Whitman, E.; Bourgeau-Chavez, L.L. Quantifying Surface Severity of the 2014 and 2015 Fires in the Great Slave Lake Area of Canada. *Int. J. Wildland Fire* **2020**, *29*, 892–906. [CrossRef]

36. Marcos, B.; Gonçalves, J.; Alcaraz-Segura, D.; Cunha, M.; Honrado, J.P. Assessing the Resilience of Ecosystem Functioning to Wildfires Using Satellite-Derived Metrics of Post-Fire Trajectories. *Remote Sens. Environ.* **2023**, *286*, 113441. [CrossRef]

37. Olthof, I.; Fraser, R.H. Detecting Landscape Changes in High Latitude Environments Using Landsat Trend Analysis: 2. Classification. *Remote Sens.* **2014**, *6*, 11558–11578. [CrossRef]

38. Miller, E.A.; Jones, B.M.; Baughman, C.A.; Jandt, R.R.; Jenkins, J.L.; Yokel, D.A. Unrecorded Tundra Fires of the Arctic Slope, Alaska USA. *Fire* **2023**, *6*, 101. [CrossRef]

39. Roteta, E.; Bastarrika, A.; Padilla, M.; Storm, T.; Chuvieco, E. Development of a Sentinel-2 Burned Area Algorithm: Generation of a Small Fire Database for Sub-Saharan Africa. *Remote Sens. Environ.* **2019**, *222*, 1–17. [CrossRef]

40. Zhang, Z.; Wang, L.; Xue, N.; Du, Z. Spatiotemporal Analysis of Active Fires in the Arctic Region during 2001–2019 and a Fire Risk Assessment Model. *Fire* **2021**, *4*, 57. [CrossRef]

41. Lizundia-Loiola, J.; Franquesa, M.; Khairoun, A.; Chuvieco, E. Global Burned Area Mapping from Sentinel-3 Synergy and VIIRS Active Fires. *Remote Sens. Environ.* **2022**, *282*, 113298. [CrossRef]

42. Ramo, R.; Roteta, E.; Bistinas, I.; van Wees, D.; Bastarrika, A.; Chuvieco, E.; van der Werf, G.R. African Burned Area and Fire Carbon Emissions Are Strongly Impacted by Small Fires Undetected by Coarse Resolution Satellite Data. *Proc. Natl. Acad. Sci. USA* **2021**, *118*, e2011160118. [CrossRef]

43. Coogan, S.C.P.; Daniels, L.D.; Boychuk, D.; Burton, P.J.; Flannigan, M.D.; Gauthier, S.; Kafka, V.; Park, J.S.; Wotton, B.M. Fifty Years of Wildland Fire Science in Canada. *Can. J. For. Res.* **2021**, *51*, 283–302. [CrossRef]

44. Stocks, B.J.; Mason, J.A.; Todd, J.B.; Bosch, E.M.; Wotton, B.M.; Amiro, B.D.; Flannigan, M.D.; Hirsch, K.G.; Logan, K.A.; Martell, D.L.; et al. Large Forest Fires in Canada, 1959–1997. *J. Geophys. Res. Atmos.* **2002**, *107*, FFR 5-1–FFR 5-12. [CrossRef]

45. Waigl, C.F.; Stuefer, M.; Prakash, A.; Ichoku, C. Detecting High and Low-Intensity Fires in Alaska Using VIIRS I-Band Data: An Improved Operational Approach for High Latitudes. *Remote Sens. Environ.* **2017**, *199*, 389–400. [CrossRef]

46. Fu, Y.; Li, R.; Wang, X.; Bergeron, Y.; Valeria, O.; Chavardès, R.D.; Wang, Y.; Hu, J. Fire Detection and Fire Radiative Power in Forests and Low-Biomass Lands in Northeast Asia: MODIS versus VIIRS Fire Products. *Remote Sens.* **2020**, *12*, 2870. [CrossRef]

47. Ju, J.; Roy, D.P. The Availability of Cloud-Free Landsat ETM+ Data over the Conterminous United States and Globally. *Remote Sens. Environ.* **2008**, *112*, 1196–1211. [CrossRef]

48. Comiso, J.C.; Hall, D.K. Climate Trends in the Arctic as Observed from Space. *WIREs Clim. Chang.* **2014**, *5*, 389–409. [CrossRef] [PubMed]

49. Li, F.; Zhang, X.; Kondragunta, S.; Csiszar, I. Comparison of Fire Radiative Power Estimates From VIIRS and MODIS Observations. *J. Geophys. Res. Atmos.* **2018**, *123*, 4545–4563. [CrossRef]

50. Giglio, L.; Descloitres, J.; Justice, C.O.; Kaufman, Y.J. An Enhanced Contextual Fire Detection Algorithm for MODIS. *Remote Sens. Environ.* **2003**, *87*, 273–282. [CrossRef]

51. Giglio, L.; Boschetti, L.; Roy, D.P.; Humber, M.L.; Justice, C.O. The Collection 6 MODIS Burned Area Mapping Algorithm and Product. *Remote Sens. Environ.* **2018**, *217*, 72–85. [CrossRef] [PubMed]

52. NASA-FIRMS. Available online: https://firms.modaps.eosdis.nasa.gov/map/ (accessed on 23 November 2023).

53. Environment and Climate Change Canada Lightning Density Data. Available online: https://open.canada.ca/data/en/dataset/75dfb8cb-9efc-4c15-bcb5-7562f89517ce (accessed on 18 December 2023).

54. Qu, Y.; Miralles, D.G.; Veraverbeke, S.; Vereecken, H.; Montzka, C. Wildfire Precursors Show Complementary Predictability in Different Timescales. *Nat. Commun.* **2023**, *14*, 6829. [CrossRef] [PubMed]

55. Rantanen, M.; Karpechko, A.Y.; Lipponen, A.; Nordling, K.; Hyvärinen, O.; Ruosteenoja, K.; Vihma, T.; Laaksonen, A. The Arctic Has Warmed Nearly Four Times Faster than the Globe since 1979. *Commun. Earth Environ.* **2022**, *3*, 168. [CrossRef]

56. Myers-Smith, I.H.; Kerby, J.T.; Phoenix, G.K.; Bjerke, J.W.; Epstein, H.E.; Assmann, J.J.; John, C.; Andreu-Hayles, L.; Angers-Blondin, S.; Beck, P.S.A.; et al. Complexity Revealed in the Greening of the Arctic. *Nat. Clim. Chang.* **2020**, *10*, 106–117. [CrossRef]

57. Jain, P.; Castellanos-Acuna, D.; Coogan, S.C.P.; Abatzoglou, J.T.; Flannigan, M.D. Observed Increases in Extreme Fire Weather Driven by Atmospheric Humidity and Temperature. *Nat. Clim. Chang.* **2022**, *12*, 63–70. [CrossRef]

58. Young, A.M.; Higuera, P.E.; Abatzoglou, J.T.; Duffy, P.A.; Hu, F.S. Consequences of Climatic Thresholds for Projecting Fire Activity and Ecological Change. *Glob. Ecol. Biogeogr.* **2019**, *28*, 521–532. [CrossRef]

59. Mack, M.C.; Bret-Harte, M.S.; Hollingsworth, T.N.; Jandt, R.R.; Schuur, E.A.G.; Shaver, G.R.; Verbyla, D.L. Carbon Loss from an Unprecedented Arctic Tundra Wildfire. *Nature* **2011**, *475*, 489–492. [CrossRef] [PubMed]

60. Stow, D.A.; Hope, A.; McGuire, D.; Verbyla, D.; Gamon, J.; Huemmrich, F.; Houston, S.; Racine, C.; Sturm, M.; Tape, K.; et al. Remote Sensing of Vegetation and Land-Cover Change in Arctic Tundra Ecosystems. *Remote Sens. Environ.* **2004**, *89*, 281–308. [CrossRef]

61. Chen, Y.; Romps, D.M.; Seeley, J.T.; Veraverbeke, S.; Riley, W.J.; Mekonnen, Z.A.; Randerson, J.T. Future Increases in Arctic Lightning and Fire Risk for Permafrost Carbon. *Nat. Clim. Chang.* **2021**, *11*, 404–410. [CrossRef]

62. Bintanja, R.; van der Wiel, K.; van der Linden, E.C.; Reusen, J.; Bogerd, L.; Krikken, F.; Selten, F.M. Strong Future Increases in Arctic Precipitation Variability Linked to Poleward Moisture Transport. *Sci. Adv.* **2020**, *6*, eaax6869. [CrossRef]

63. Yoseph, E.; Hoy, E.; Elder, C.D.; Ludwig, S.M.; Thompson, D.R.; Miller, C.E. Tundra Fire Increases the Likelihood of Methane Hotspot Formation in the Yukon–Kuskokwim Delta, Alaska, USA. *Environ. Res. Lett.* **2023**, *18*, 104042. [CrossRef]

64. DeVries, B.; Pratihast, A.K.; Verbesselt, J.; Kooistra, L.; Herold, M. Characterizing Forest Change Using Community-Based Monitoring Data and Landsat Time Series. *PLoS ONE* **2016**, *11*, e0147121. [CrossRef]